Engineering Fracture Mechanics 248 (2021) 107713

Contents lists available at ScienceDirect

Engineering Fracture Mechanics

journal homepage: www.elsevier.com/locate/engfracmech

Fatigue strength of rebars embedded in concrete—A numerical approach

Iris Luijters [a], Johan Maljaars [a,b,*], Simon Wijte [a]

[a] Eindhoven University of Technology, The Netherlands
[b] TNO, The Netherlands

ARTICLE INFO

Keywords:
Reinforcement bar
Fatigue
Concrete-steel bond
Fracture mechanics
Stress concentration factor
Stress intensity factor

ABSTRACT

The effect of embedding in concrete on the fatigue performance of steel reinforcement bars is not evident. Some test series provided in literature demonstrate a higher fatigue resistance of embedded bars as compared to bars in air, whereas others provide a lower resistance. In addition, debate exists on the mechanisms behind the difference between tests in air and tests in concrete, if any. These mechanisms mentioned in literature are empirically based. This paper provides a numerical (finite element) study on the stress concentration factors and the stress intensity factors for the two conditions. It shows that the locations of cracks in concrete relative to the ribs on rebars and the distance between concrete cracks have little influence on the stress peaks in the rebar and hence on the fatigue performance of the rebar. Mechanical interlock or pressure of concrete against the ribs slightly contributes to the rebar stress concentrations. No significant difference should be expected in fatigue resistance between rebars in air and rebars embedded in concrete. Variations in local geometry at the root of ribs appear of more significant influence.

1. Introduction

Extensive experimental campaigns have been devoted to the fatigue performance of steel reinforcement bars (rebars), e.g. [1–4]. The typical fatigue strength expressed as stress range of ribbed reinforcing bars is between 150 and 280 N/mm^2 at 1 million cycles, [5]. These studies showed that this large variation is caused by the aspects: stress ratio R, bar diameter D, steel grade, marking of the bars if any, (corrosive) environment, presence of welds, pre-bending of the bars, and presence of ribs (also called lugs). With respect to the rib dimensions, Fig. 1, it appears that transverse ribs with a small base radius over rib height r/h, steep flank angles α, and large base width w, result into relatively large stress concentrations and therefore relatively short lives.

The studies mentioned before are done on axially loaded single rebars that are not embedded, generally referred to as 'tested in air'. Fewer studies are devoted to the fatigue performance of rebars embedded in concrete, the most extensive one being [7]. Experimental campaigns – often with relatively small number of tests specimens – compared the fatigue strength of reinforcing bars in air with bars embedded in concrete. Conflicting results are obtained on the influence of concrete embedment, see the overviews in [8] and [5]:

Moss [9] conducted experimental research on the fatigue strength of reinforcing bars in air and embedded in concrete, see Fig. 2. The fatigue resistance of 16 mm diameter ribbed bars, embedded in a concrete beam and tested in bending, was approximately 20% higher than that of the same bars tested in air and loaded axially. Fatigue failure of the rebars was found to always coincide with a crack in the concrete that was formed at the first load cycle. The crack initiation site was associated with the pattern of ribs.

* Corresponding author at: Eindhoven University of Technology, The Netherlands.
E-mail address: johan.maljaars@tno.nl (J. Maljaars).

https://doi.org/10.1016/j.engfracmech.2021.107713
Received 25 October 2020; Received in revised form 12 March 2021; Accepted 24 March 2021
Available online 1 April 2021

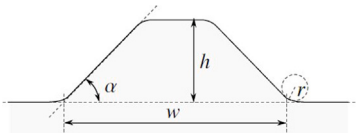

Fig. 1. Rebar rib dimensions with cross-section perpendicular to rib, [6].

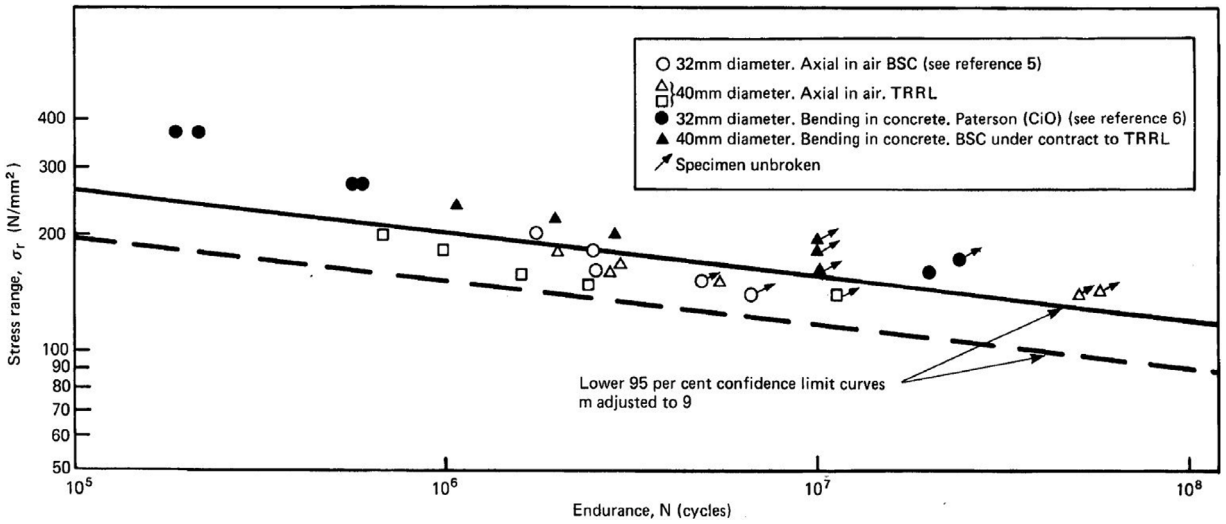

Fig. 2. Moss' fatigue test results of large diameter rebars in air and in concrete.
Source: Reprint from [9].

Moss recommended that the fatigue properties of reinforcement for design purposes should be assessed from axial tests, since the beneficial effect of the embedment in concrete may vary between structures due to differences in concrete strength, concrete cover, and other parameters.

Similar to the study of Moss, also the experimental studies of Jhamb and MacGregor [10] and Soretz [11] provided an increase in the fatigue resistance of ribbed rebars of 7% and between 10% and 20%, respectively, when embedded in concrete as compared to axial loading in air. Conflicting results where obtained by Rehm [12] and Westerberg and Jacobson [13], who observed a reduced fatigue resistance when embedded in concrete in their experimental campaigns. Tilly [14] compared concrete beam tests in [15] with axially loaded specimen in air of [16] and concluded that there is no significant difference in fatigue life between the two cases. Soltani et al. [4] tested two reinforced concrete beams, of which one failed. The fatigue resistance of this single test corresponded to that of rebars tested in air.

The following explanations have been provided for a potential better performance when embedded in concrete:

i The weakest link principle applies to fatigue, where the probability of a fatigue crack is highest at largest notch combined with the largest local stress. In air, the nominal stress σ – i.e. average stress over the cross-section – is equal over the bar length and hence the rib with the largest notch effect is decisive. In concrete, rebar stresses are larger than average in the vicinity of a concrete crack and lower elsewhere. The probability that the weakest location in the rebar coincides with the concrete crack location is small, [11,14]. Moss [9] reports that the embedded rebar in tests always failed at the position of a crack in the concrete, which had formed at the beginning of the test.

ii The efficiency or stiffness of the bond between concrete and steel is not considered in the calculation of the stress range in the rebar, whereas it has been demonstrated to reduce the local stress range in tests [11] or simulations [8].

iii Grains in the concrete crack may prevent the crack from complete closure at minimum load. In addition, local slip may occur between concrete and rebar at the concrete crack. Both aspects cause the minimum stress level in the rebar to be larger and hence the stress range to be smaller than in a calculation in which these aspects are not considered, [11].

iv The concrete beam tested in bending causes a stress gradient in the rebar. A defect in the rebar gives a longer life if it is located at a fibre experiencing lower than average stress, [9].

A potentially worse performance when embedded in concrete is attributed to the following, [13]:

i Similar to the last mentioned cause of better performance, a defect located at a fibre experiencing higher than average stress gives a relatively shorter life.

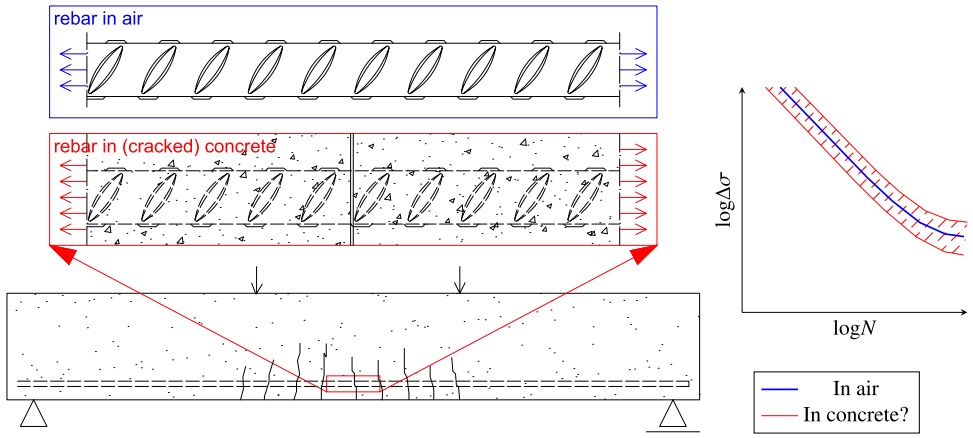

Fig. 3. Outline of the paper — is the fatigue resistance of rebars in concrete better or worse than in air?

ii Local curvature of the rebar occurs at the concrete cracks, thereby contributing to a non-uniform stress distribution over the rebar cross-section.

iii Concrete pressing against the ribs causes a higher stress concentration at the rib root as compared to a continuously loaded rebar in air.

The majority of this research stems from around 1980. Different from prestressing strands, where much more recent studies have been performed and have led to the consensus that embedded prestressing strands have a worse fatigue resistance as compared to strands in air, [17], the issue of fatigue of embedded reinforcing bars remains unsolved to date. This may be related to the small number of reported fatigue failures of reinforcement in actual structures. More recently, however, fatigue is mentioned as a potential cause of failures of concrete wind turbine foundations, e.g. [18,19]. In addition, because of the increasing age of many reinforced concrete bridges or bridge slabs and the large increase of heavy vehicle crossings since their design, [20], a number of road and rail authorities have expressed their concern about this potential failure mode. Finally, the benefits of increasingly stronger concrete mixtures and reinforcement bars are at certain point limited by the fatigue resistance. For such cases, it is relevant to know if the large database of fatigue tests in air is also representative for the embedded condition and forms the motivation for the current study.

The small number of tests per series on concrete beams and the difference in dimensions of these between the series complicates the evaluation of the effect of concrete embedment on the fatigue resistance of rebars. Simulations using the finite element method (FEM) may give insight into the different aspects that contribute to the fatigue resistance of rebars. Several studies are conducted into the stress concentration occurring at the rib root of rebars. Jhamb and McGregor [10] and Rocha Rocha Pinto Portela Nunes [6] used the FEM to evaluate the effect of rib dimensions on the stress concentration factor (SCF). Their findings agree with the experimentally determined parameters of importance in [3], as indicated at the start of this section. A similar study was conducted in [21], where a good correlation was obtained between the stress concentration determined with the FEM and the fatigue resistance determined in experiments. These studies considered rebars in air. To the authors' knowledge, studies have not been conducted where the influence of concrete embedment on the stress concentrations of rebars was evaluated through FEM.

Daoud and Lovegrove [8] studied the effect of concrete bond on the stress intensity factor (SIF) of an edge crack in reinforcement bars by making use of the FEM. The SIF was evaluated in a simplified two-dimensional model for an edge crack in a smooth bar – i.e. a bar without ribs – embedded in a concrete beam. It was concluded that the SIF of a bar with crack embedded in concrete with full bond between the materials was significantly lower than that of a bar in air with the same crack, for crack depths of $a > 0.15D$, but slightly higher for smaller depths. Partially bonded rebars were in between these two extremes. The results qualitatively agreed with the results of an earlier study by Lovegrove et al. [22], who have measured the number of cycles to failure of four specimens, comprised of initially notched bars without ribs embedded in concrete beams. They compared their results with fatigue crack growth rates measured in steels of comparable strength in [23] and concluded that the crack growth rate of bars in concrete is lower as compared to bars in air for SIF up to 25 MPa $m^{1/2}$. To the authors' knowledge, studies to the crack growth rate or SIF of rebars with ribs embedded in concrete have not been performed before.

The objective of the current study is to contribute to the understanding of differences between fatigue of rebars in air and in concrete, if any, and to evaluate the different explanations provided in literature for the differences by making use of the FEM, Fig. 3. The approach followed here allows for an analysis of the role of concrete embedment on the fatigue relevant stress distributions in rebars with ribs, with a level of detail that has not been considered before. Sections 2 and 3 provide the models and results related to the SCF and SIF in air and embedded in concrete, respectively. An estimate of the fatigue initiation and propagation lives based on the SCF and SIF results, respectively, forms the subject of Section 4. Section 5 presents a discussion of the results.

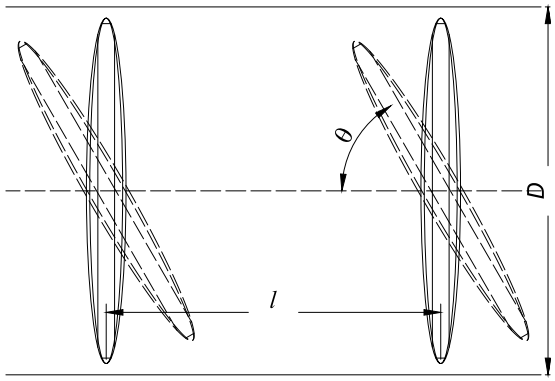

Fig. 4. Definition of rib angle, θ, and rib distance, l.

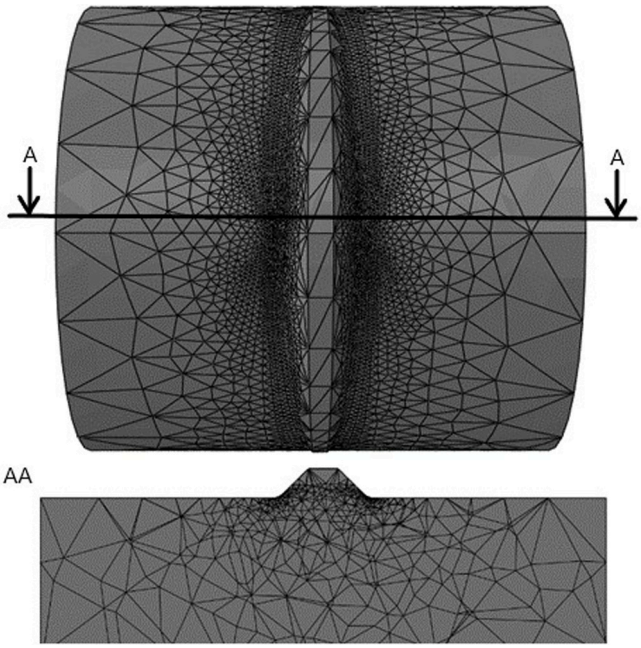

Fig. 5. Solid element model with unstructured mesh in FEM of a rebar in air with $r/h = 0.1$.

2. Models of rebars in air

2.1. Stress concentration factors

Rebars are considered with a diameter of $D = 24$ mm including ribs with dimensions according to Figs. 1 and 4 of $l/D = 10/24$, $h/D = 1/24$, $h/w = 1/3$, $\alpha = 45°$, $\theta = 90$, 60 or 45°, and $0.1 \leq r/h \leq 1.0$. Hence, the relative rib radius is varied as it appears the dominant variable for the SCF according to [1,21,24,25]. A limited number of rebars with $\alpha = 65°$ are analysed to study its influence. These dimensions meet the requirements of standard [26]. All finite element models are constructed in Abaqus/CAE 6.14 software.

A finite element model of a rebar in air is constructed using C3D10 s order tetrahedron elements containing 10 nodes and 4 integration points. The applied Young's modulus and Poisson ratio are $E = 2.1 \times 10^5$ N/mm^2 and $\nu = 0.3$, respectively. A non-structured mesh is selected for this solid model, see Fig. 5. Symmetry conditions are applied on one end of the model and a uniform tensile stress is applied on the other end (left and right sides in the figure). The SCF, K_t, is defined as the maximum principal stress at the surface, σ_p, divided by the applied stress, σ:

$$K_t = \sigma_p/\sigma \tag{1}$$

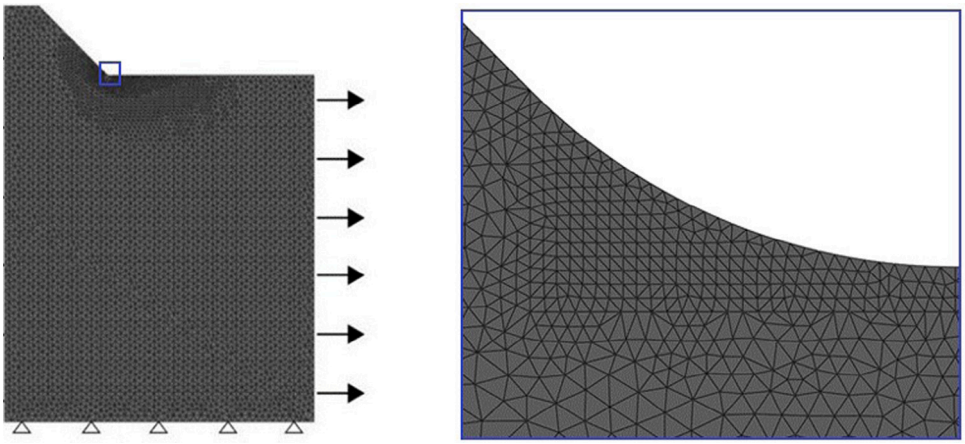

Fig. 6. Part of the axi-symmetrical model with structured mesh of a rebar in air, $r/h = 0.1$.

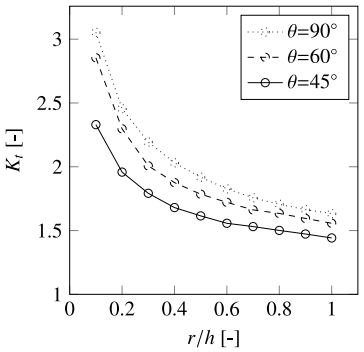

Fig. 7. SCF of rebars in air with $D = 24$ mm and with various rib angles and root radii.

The required mesh size near the rib root and the required model length are determined in a sensitivity study. A mesh size of 0.01 mm near the point of interest appears (more than) sufficient to reach convergence for all geometries considered. The SCF in a model with length l equal to the rib spacing (Fig. 4), i.e. containing one rib in the centre and with symmetry boundary conditions on one end and a uniform tensile load on the other end, appears to be (almost) equal to the SCF in a model with length $6l$, containing six ribs. For this reason, the model used to determine the SCF in air has length l. To verify the performance of the non-structured mesh, the SCF of the model with $\theta = 90°$ is compared to that of two axi-symmetrical models: One with a similar, unstructured mesh as the solid model and triangular elements of type CAX6M and the other with a very dense structured mesh of quadrilateral elements type CHX8. Fig. 6 shows the model with structured mesh.

The SCF of the axisymmetrical model with unstructured mesh is equal (difference less than 0.1%) to that of the structured mesh. This SCF is 1% lower as compared to the SCF in the axisymmetrical model of [21]. The SCF in the axi-symmetrical model is between 3% and 4% lower than that of the solid model for the entire range of $0.1 \leq r/h \leq 1.0$. The difference between the axi-symmetrical and the solid element model is attributed to the rib in the axisymmetrical model being continuous along the perimeter of the bar, i.e. a small difference with the actual rib applied in the solid model. Based on the comparison, the solid model with unstructured mesh is considered sufficiently accurate for the purpose of this study.

Fig. 7 provides the SCF as a function of the relative rib radius, r/h, and the rib angle, θ. The figure demonstrates a large influence of the relative radius; i.e. a small radius results in a relatively large SCF and this is expected to result into a relatively low fatigue life. Such an influence is expected from a geometric consideration, i.e. a small radius gives a sharp geometrical discontinuity, but it is remarkable because international product standards such as [26] do not provide requirements on the (relative) rib radius. The rib angle also appears of importance, but less so as compared to the relative radius. This agrees with the observations from a FEM study in [6]. The highest SCF of rebars with a rib angle of $\theta = 90°$ is at the centre of the rib. This position shifts towards the end of the rib as θ decreases, see Fig. 8.

In addition to the SCF, the gradient of the stress is known to be relevant for the fatigue resistance, [27]. The stress gradient, G, is defined according to [28]:

$$G = \frac{\sigma_p - \sigma_\delta}{\sigma_p} \frac{[mm]}{\delta} \tag{2}$$

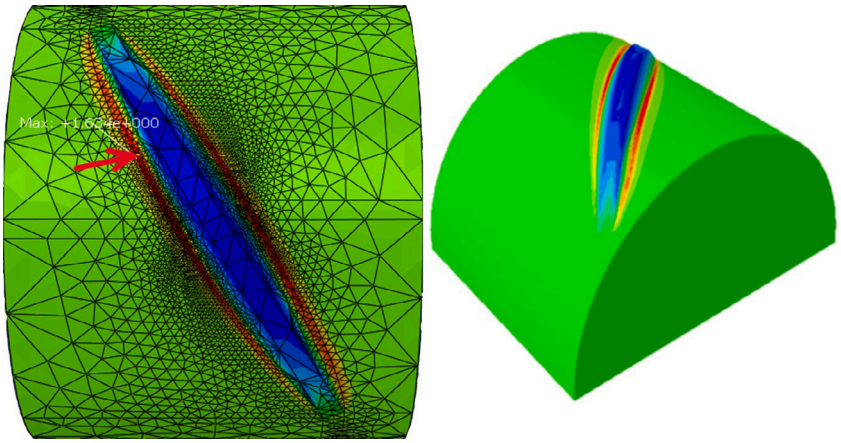

Fig. 8. Contour plot (normalized stress, green = nominal, red = 2 x nominal, blue = 0) of a rebar in air with $\theta = 60°$, $r/h = 0.5$. Red arrow shows maximum stress location.

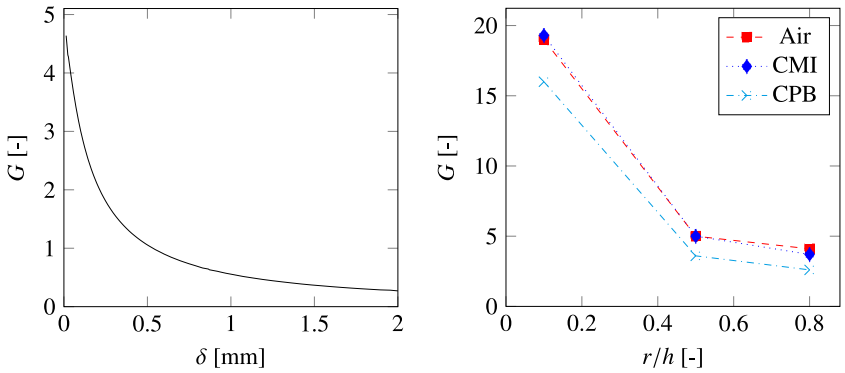

Fig. 9. Stress gradients of rebars with $\theta = 90°$: (a) G (Eq. (2)) as function of δ for a bar with $r/h = 0.5$ and CMI; (b) G at $\delta \approx 0$ for different geometries and bond conditions.

where σ_δ is the principal stress at a distance δ below the surface from the location of σ_p. The stress gradient in round bars is not constant but depends on δ, see Fig. 9a. Extrapolation of the relation to the surface of the bar gives a value of G that can be reasonably approximated by taking the stress σ_δ very close to the surface, e.g. at $\delta = 0.01$ mm, equal to the mesh size in the current study. This distance is used to evaluate G. The red squares in Fig. 9b provide the stress gradient for three relative rib radii of rebars in air (other data are introduced below). Obviously, the largest SCF are accompanied by the largest gradients.

2.2. Stress intensity factors

Fatigue of metals is the process of initiation and subsequent propagation of discrete cracks. For considering crack propagation, such a discrete crack has therefore been introduced in the model of the rebar at the location of maximum stress concentration. The SIF is determined for a limited set of parameters, namely $\theta = 90°$ and $r/h = 0.5$. It is not known – at least not a priori – how a crack in a bar with a rib at a different angle than $\theta = 90°$ grows. It is expected to follow the rib root at small size but to grow perpendicular to the stress direction at larger size, but the size at which this transition occurs is unknown. The models used to determine the SIF contain six ribs (model length = $6l$). A semi-elliptical crack is applied near the location of the maximum stress of the centre rib. The crack front is modelled with a spiderweb mesh, containing four layers of hexahedron elements and one layer of collapsed hexahedron elements of type C3D20. Midpoint nodes in the collapsed elements are shifted to quarter point position. Fig. 10a provides a view of the spiderweb mesh around the crack front. This part was inserted into the model of the rebar. The logical location for a crack to initiate is at the point of maximum stress. This point is in the rib root radius. However, the spiderweb mesh around the crack front could not be inserted in the rib root for reasons of mesh compatibility. For this reason, the crack was shifted 0.3 mm away from the root, see Fig. 10b, in which the red cross indicates the location of maximum stress. This may slightly influence the SIF at the surface point, but is not expected to influence the SIF at the deepest point of the crack.

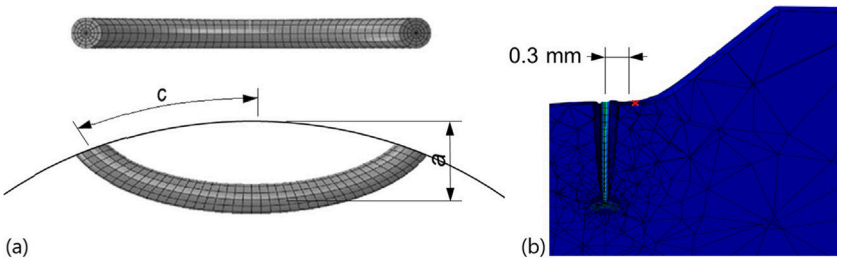

Fig. 10. Crack front mesh: (a) Spider mesh; (b) Crack surface point relative to rib root.

The SIF is obtained with the concept of the J-integral, using the third contour. All results are presented as the geometrical correction factor, Y, defined as:

$$Y = \frac{K}{\sigma\sqrt{\pi a}} \tag{3}$$

where:

K = Stress intensity factor

σ = Stress

a = Crack depth in the rebar

Round rebars without ribs are also modelled and values of Y compared to data from others as a check of the model. Forman and Shivakumar [29] have obtained the following equation for Y of semi-circular cracks in round bars:

$$Y = \frac{1.84}{\pi\cos\left(\frac{\pi a}{2D}\right)}\sqrt{\frac{\tan\left(\frac{\pi a}{2D}\right)}{\frac{\pi a}{2D}}}\left(0.752 + 2.02\frac{a}{D} + 0.37\left[1 - \sin\left(\frac{\pi a}{2D}\right)\right]^3\right) \tag{4}$$

The equation gives a good fit of the average data obtained from various studies at the deepest point and at the surface, with a scatter between these studies of approximately 15%, [30]. Geometrical correction factors of semi-elliptical cracks in round bars are given in [31] for five different crack depths and three crack aspect ratios a/c, where c is the semi crack length measured around the perimeter of the bar, see Fig. 10. Assuming that one single crack growth relationship applies, a fatigue crack grows to a condition where K (and hence Y) is equal along the crack front. The difference in Y between the surface point and the deepest point in [31] for $a/c = 1$ therefore demonstrates that the optimum shape of the crack front is not semi-circular. The optimum is estimated here by linear interpolation between the aspect ratios in [31] in such a way, that Y in the deepest point is equal to that at the surface. With the optimum aspect ratio obtained in this way, Y of the deepest point in [31] is on average 7% higher than the solution for semi-circular cracks of Eq. (4).

The current model is modified to a round bar and compared to the solutions in [29] and [31] for a crack with a relative depth of $a/D = 0.25$. The geometrical correction factor, Y, for a semi-circular crack is 3% lower with the current model as compared to Eq. (4). The optimum aspect ratio obtained through trial and error with the current model is $(a/c)_{opt} = 0.70$, whereas it is 0.73 when using linear interpolation between the values of [31]. (Tests in [29] give $0.83 < (a/c)_{opt} < 0.95$ at similar relative crack depths). The geometrical correction factor, Y, for a semi-elliptical crack with optimum aspect ratio is 3% higher with the current model as compared to the interpolated values of [31]. Hence, the model is considered sufficiently accurate for the purpose of the current study.

Bars with ribs are subsequently studied. The continuous curve in Fig. 11 provides Y as a function of the relative distance along the crack front, x/d, Fig. 11, for a semi-circular crack with $a/D = 0.25$. The black dots present data from [31] for a round bar. The two solutions are equal for the deepest point of the crack but, not surprisingly, the presence of the rib causes a higher SIF at the surface point of the crack. In this study, the optimum aspect ratio is considered as the aspect ratio at which the average SIF along the crack front is equal to the SIF in the deepest point of the crack. This appears to be $(a/c)_{opt} = 0.70$ for the crack with $a/D = 0.25$, Fig. 11.

The red curve and boxes in Fig. 12 provide the optimal aspect ratio and the corresponding geometrical correction factor of cracks with different depths in rebars with ribs in air. The optimal aspect ratio is similar to the one of round bars without ribs according to [31] (black curve with dots). The presence of the rib causes an increase in Y for small relative crack depths but the influence decays for larger depths, similar to the influence of threads in threaded bars, [30]. The geometrical correction factor of relatively deep cracks according to the current model with ribs appears lower than those for round bars of [31] and [29]. This difference may be caused by different interpretation of data, where the current evaluation provides the average value of Y along the crack front (again, equal to the value in the deepest point). An expression for Y is obtained by curve-fitting the data using a similar expression as [30] applied for threaded bars, i.e. an expression for a round bar together with an exponential correction factor that considers the influence of the rib. The correction factor is expected to scale with the SCF, i.e. a higher SCF gives a larger SIF for near surface cracks. The geometrical correction factor for rebars with ribs in air containing semi-elliptical cracks is:

$$Y = \frac{(K_t - 1)}{c_1}\exp\left(c_2\frac{a}{D}\right) + c_3 + c_4\frac{a}{D} + c_5\left(\frac{a}{D}\right)^2 + c_6\left(\frac{a}{D}\right)^3 + c_7\left(\frac{a}{D}\right)^4 \tag{5}$$

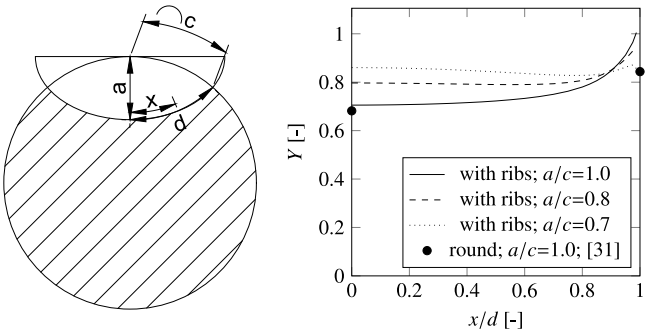

Fig. 11. SIF along the crack front of bars in air with $a/D = 0.25$.

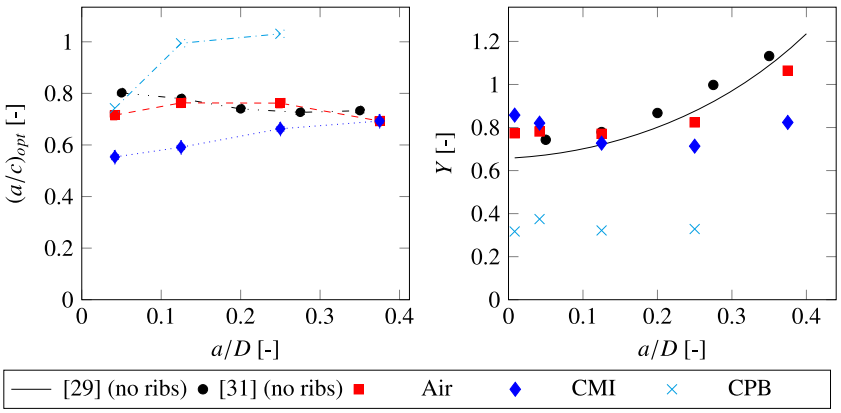

Fig. 12. Simulation results of bars containing cracks: (a) optimal aspect ratio of the crack; (b) corresponding geometrical correction factor of the SIF.

where coefficients $c_1 = 4$ and $c_2 = -20$ are fit to the available data for ribbed rebars in air and $c_3 = 0.6507$, $c_4 = 0.5367$, $c_5 = 3.0469$, $c_6 = -19.504$ and $c_7 = 45.647$ are coefficients according to [30] for a round bar containing a crack front that transits from semi-circular for shallow cracks to straight-fronted for deep cracks. As the exponential correction factor is based on limited data, this equation provides an estimate only.

3. Models of rebars in concrete

3.1. Bond stiffness

Five standard pull-out tests according to [26] are carried out to determine the stiffness of the bond between steel and concrete. In each test, a rebar with $D = 12$ mm and an anchor length of $5D$ is pulled out of a concrete block with dimensions $200 \times 200 \times 200$ mm^3, while the load F and the extensions at the loaded side Δp and the unloaded side Δq are measured, see Fig. 13(a). The force–displacement curves of Fig. 13(b) plot Δp and Δq with positive and negative values, respectively. The shape of the curves agree with that of others, e.g. [32]. Because forces in fatigue generally remain in the elastic range, only the linear part of the force–extension diagram is considered, Fig. 13(c). The appropriateness of this assumption is checked hereafter.

The theoretical bond stiffness, defined as the ratio between the theoretical shear stress and the deformation, cannot be applied in the model because it implicitly accounts for mechanical interlock through the ribs whereas the latter aspect is modelled explicitly here. Instead, the bond between concrete and steel is modelled as a cohesive surface at the interface with a stiffness obtained in Abaqus through trial. The exact geometry of the test specimen is modelled – including the ribs and the concrete block, see Fig. 14 – and the force–extension diagram is determined and compared to the test. The same types of element as previously described are used. The elastic properties applied in Abaqus for concrete are taken from additional tests with the same concrete mix and are $E = 2 \times 10^4$ N/mm^2 and $\nu = 0.2$. The constant elastic cohesive shear stiffness, k, defined as the ratio between the traction and the displacement, accounts for the effects of friction between the materials, for micro cracking that may occur in concrete near the ribs, and for local variations of the concrete Young's modulus at the interface. By calibrating the cohesive shear stiffness to match the pull-out tests, these aspects are incorporated in a phenomenological manner. At very low stress levels the cohesive stiffness also considers the effects of adhesion (or chemical bonding) between the two materials, but the chemical bond may be assumed as broken at the stress levels relevant to fatigue. Moreover the experimental force–displacement curves show a single linear branch instead

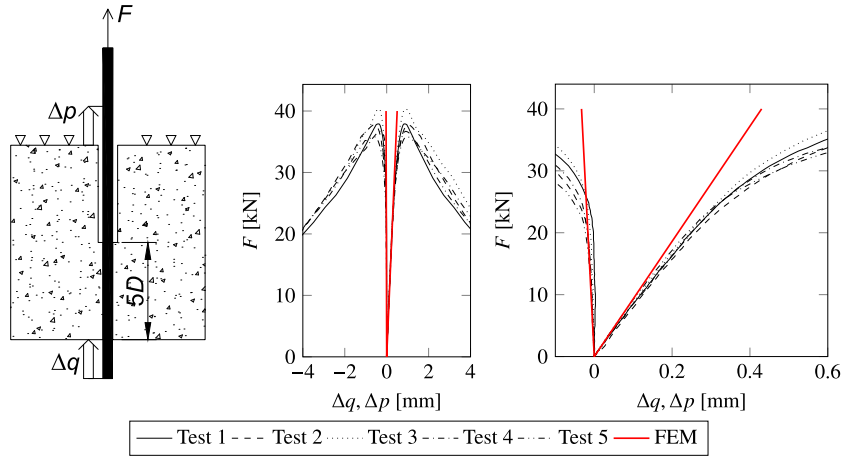

Fig. 13. Set-up and results of the pull-out tests (black) and FEM (red): (a) Schematic test set-up; (b) Force–displacement curves; (c) Zoom of force–displacement curves for small deformations.

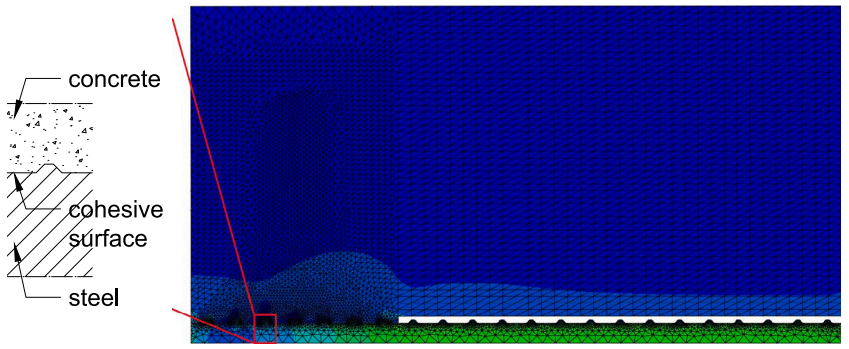

Fig. 14. Cross-section of the model of the pull-out tests.

of two branches, so chemical bonding is apparently not so relevant for the stiffness. The simulations with $k = 600$ N/mm^3 give a reasonable agreement with the force–displacement curves of the tests; the deformation is slightly overestimated at the unloaded side and slightly underestimated at the loaded side, see the red lines in Fig. 13.

Two trial values are selected for the normal stiffness of the cohesive surfaces namely, equal to 0 and equal to the shear stiffness $k = 600$ N/mm^3. The latter stiffness gives a 6% larger deformation and a 1% smaller SCF as compared to the former. It is concluded that the cohesive normal stiffness is unimportant for the aim of this study. Note that pressure overclosure is active, preventing penetration of the meshes of rebar and concrete.

The actual bond stiffness may vary along the rebar and be different at ribs and between ribs. In addition, the monotonic bond stiffness may deteriorate due to fatigue, [33,34]. The mentioned value of $k = 600$ N/mm^3 should therefore be treated as an approximation. For this reason, simulations are also carried out with the two extremes:

- Complete composite working where the nodes of the rebar are equal to those of the concrete at the interface, i.e. $k = \infty$, hereafter referred to as "Concrete, Perfect Bond (CPB)".
- No friction, i.e. $k = 0$, referred to as "Concrete, Mechanical Interloc (CMI)".

3.2. Stress concentration factors

Moss [9] observed cracks in the concrete beams in his fatigue tests at the application of the first load cycles. The final fracture of the bar occurred at the (approximate) same location as one of these concrete cracks. Nagesh and Appa Rao [35] observed concrete cracks after less than 0.6% of the total number of cycles causing fracture of the rebars in their constant amplitude loads. No significant alteration of the crack pattern was observed at further cycling. Hence, one can assume concrete cracks being present during the entire fatigue process in the fatigue tests and it is not necessary to model the concrete fracture process. For this reason, a model was constructed containing a discrete crack (modelled as a seam) arbitrarily ending halfway between two ribs, where the rebar transfers the tensile forces at the concrete crack, see Fig. 15. The model is aimed to represent the tension side of a concrete beam. The concrete block has dimensions of 200 × 200 mm^2 and the distance considered between the concrete cracks is 120 mm

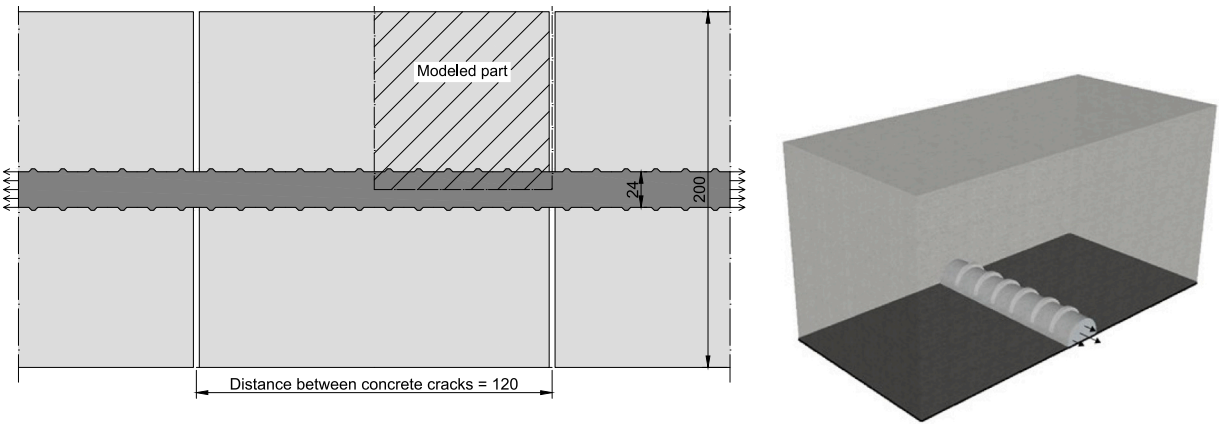

Fig. 15. Schematic of the model of the rebar embedded in cracked concrete (dimensions in mm, not on scale).

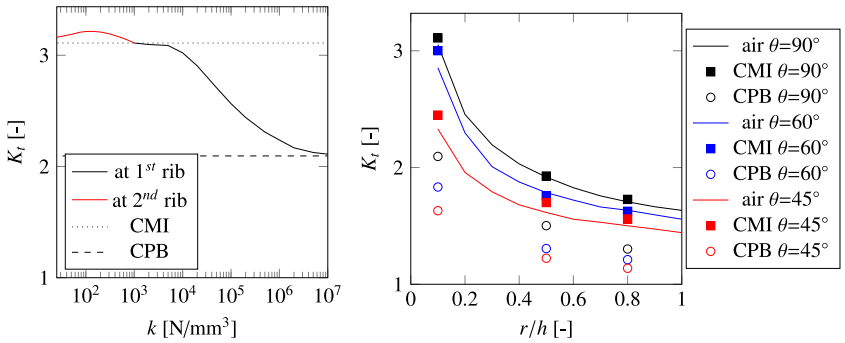

Fig. 16. SCF resulting from the models: (a) SCF as function cohesive stiffness for $r/h = 0.1$ and $\theta = 90°$; (b) SCF of bars in air and in concrete.

or $5D$, spanning 12 ribs. The Young's modulus applied for concrete is $E = 3 \times 10^4$ N/mm^2. Use has been made of symmetry. This model was applied to determine the SCF.

As for the rebar in air, an axisymmetrical model with a structured mesh and a three-dimensional model consisting of solids with an unstructured mesh are analysed with the same types of element as previously described. The two models render approximately the same SCF for rebars with $\theta = 90°$ (average difference of 2%). The average shear stress in the models over a distance l measured from the concrete crack – containing one rib – at fatigue relevant stress levels of up to 400 MPa, is compared with the theoretical bond stress from the pull-out tests. In all cases the average shear stress remained in the linear range of the tests. This confirms that the cohesive surface (between the concrete tensile cracks) can indeed be modelled as elastic.

Highest SCF is observed at the rib root in all simulations, i.e. at the same location as for rebars in air, and not at the concrete crack. This indicates that the location of the concrete crack – whether ending in between ribs or at the rib root – is not so important for the fatigue performance of the rebar. This is further substantiated by two additional simulations with $r/h = 0.5$ and $\theta = 90°$ in which the concrete crack is applied at the rib root, i.e. at the location of the peak stress (without using symmetry), and 0.3 mm away from the end of the rib root. The SCF in these models is 5% or 2% higher, respectively, as compared to the model with the crack centred between two ribs, in case of a cohesive stiffness of $k = 600$ N/mm^3. In case of CMI the SCF is independent of the location of the concrete crack. The distance between the concrete cracks also appears relatively unimportant. Models with two times shorter or longer concrete crack distances than $5D$ predict an SCF that is between 3% and 7% higher or lower, respectively, than the $5D$ concrete crack model.

The black curve in Fig. 16a gives the SCF as a function of the cohesive stiffness at the rib closest to the concrete crack for a model with $r/h = 0.1$ and $\theta = 90°$. The results including cohesive stiffness origin from the axisymmetrical model to reduce the numerical complexity. CMI and CPB simulations are done with the solid element model. As expected, the SCF is bounded between the CMI and CPB simulations (dashed curves). However, the SCF at the adjacent rib, i.e. one rib away from the concrete crack, appears slightly higher for $k < 1000$ N/mm^3 (red curve in the figure). Pressure between concrete and the rib flank is highest at that location and together with the cohesive stiffness this creates friction, causing a high force transfer at the rib and hence a higher SCF than in the CMI simulation. Balázs [36] also found that a too intensive bond between steel and concrete may cause high stress concentrations. However, the difference remains small. The SCF at $k = 600$ N/mm^3 is 2% larger than in the CMI simulation. This small difference is ignored hereafter and results are provided for CMI and CPB simulations.

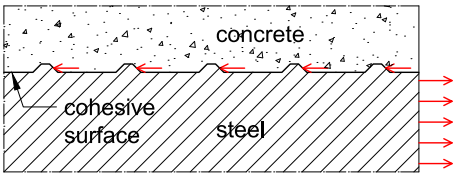

Fig. 17. Action of concrete pressing against the rebar ribs.

Fig. 16b provides the SCF resulting from the model. The data for air are equal to those in Fig. 7. The figure indicates that the SCF in simulations with a rebar embedded in concrete and without bond stiffness (CMI) is equal to or slightly higher than the SCF in air. The force transfer of concrete pressing against the ribs causes this slightly increased peak stress, Fig. 17. The theoretical case of perfect bond between steel and concrete (CPB) gives a substantially lower SCF. The difference in Young's modulus between steel and concrete causes the remaining SCF in that case. Fig. 9 provides the stress gradients for the three cases. It is obvious that the larger K_t, the larger is G.

3.3. Stress intensity factors

SIF values are obtained in a similar way as for rebars in air, but with the model explained in Section 3.2. A crack in the rebar is applied at the rib closest to the concrete crack, because concrete is expected to crack once a crack develops in the rebar. Bond stiffness is not considered for the same reason, however, data for CPB are given for reasons of comparison. Fig. 12 provides the optimal aspect ratio and the geometric correction factors for the three cases. The optimal aspect ratio of the rebar embedded in concrete and without bond stiffness (CMI) is initially smaller than that of a rebar in air, but it approaches the same ratio for deeper cracks. CMI provides a slightly higher SIF for $a/D < 0.1$ and a lower SIF for $a/D \geq 0.1$ as compared to the rebar in air. The reason for the higher SIF at small crack size is the same as for the higher SCF: the rib is slightly more severely stressed in CMI compared to air as caused by concrete pressure. The lower SIF at large cracks can be explained through the support provided by the concrete against out-of-plane (opening mode) displacement of the steel at the crack location. This restraining influence is expected to remain present once concrete cracks at the same location of the crack in the rebar. The SIF therefore tends to that of an embedded crack for large crack sizes. A lower crack growth rate in concrete as compared to air was also experimentally observed in [22] for bars without ribs that contained an initial V-shaped notch. The embedment effect is even more dominant in CPB, resulting in a low SIF, very close to that of an internal, circular crack in an infinitely large homogeneous medium, with a value of $Y = 0.4$, [37]. An approximate fit equation is formulated for CMI, based on the same considerations as for the rebar in air:

$$Y = \frac{(K_t - 1)}{c_1} \exp\left(c_8 \frac{a}{D}\right) + c_9 + c_{10}\left(\frac{a}{D}\right)^2 \tag{6}$$

where coefficients $c_1 = 4$, $c_8 = -10$, $c_9 = 0.65$ and $c_{10} = 1.1$ are fit to the data available for CMI. Again, the equation is based on limited data and hence provides an estimate only and it is valid up to approximately $a/D = 0.5$.

4. Estimate of the fatigue resistance

SCF and SIF can be considered as indicators for the crack initiation and propagation lives, respectively. The slightly higher value of the SCF for the embedded rebar with realistic bond or with no bond stiffness as compared to air suggests that the crack initiation life of an embedded rebar may be slightly lower as compared to that of a rebar in air, whereas the lower SIF for large cracks of an embedded rebar may result in a larger propagation live for large cracks, i.e. in the last stage of crack propagation, as compared to a rebar in air. The SIF and SCF values of the previous sections are used here to estimate the fatigue life. The fatigue life prediction model employed is the same as used in [38] and [39], and it is a slightly modified version of the more original model in [40], all used to predict the life of hot riveted joints. The main equations and variables are summarized in the Appendix of the current paper. The prediction model consists of the method of critical distances [41] to determine the cyclic strain from $\Delta\sigma$, K_t, and G, which is subsequently applied in the Basquin-Coffin-Manson fatigue life model [42,43] with Morrow's correction for the mean stress effect [44] for the estimate of the initiation life. The propagation life is estimated using the SIF and a variant of Paris' equation in [37]. Propagation is assumed to start at a crack depth of 0.5 mm because the parameters of the Coffin–Manson relation have been calibrated in tests with a crack size of approximately that size, see the Appendix. Propagation is simulated up to a relative crack size of $a/D = 0.5$, after which a large growth rate or fracture is assumed. As a comparison, rebar fracture occurred at a relative crack size of approximately $a/D = 0.6$ in fatigue tests in [35] on embedded rebars subjected to a stress range of 300 N/mm^2.

As an example, Fig. 18 provides the relative crack depth versus fatigue life in numbers of cycle, N, for rebars in air and for CMI, with stress range $\Delta\sigma = 250$ N/mm^2, stress ratio $R = 0.2$, rib angle $\theta = 45°$ and relative root radius $r/h = 0.5$. The figure demonstrates that the crack is predicted to grow progressively as the crack size increases, both in air and in CMI, indicating that the assumed crack depth at the end of life of $a/D = 0.5$ is not important for the fatigue life prediction. The figure demonstrates that the predicted

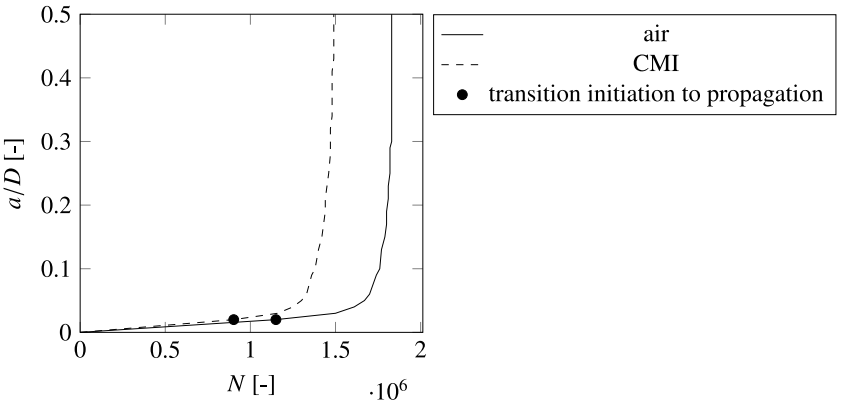

Fig. 18. Predicted fatigue life for $\Delta\sigma = 250$ N/mm^2, $R = 0.2$, $\theta = 45°$, $r/h = 0.5$.

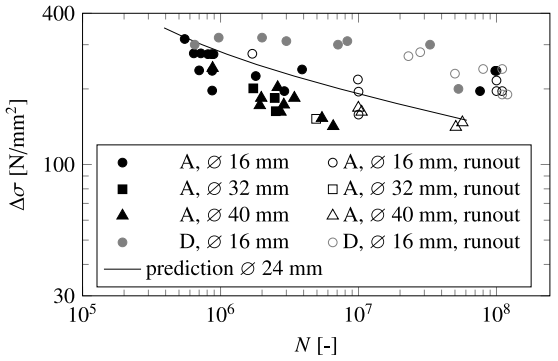

Fig. 19. Fatigue test data [45] and model prediction for rebars in air with $R = 0.2$.

life in CMI is 20% shorter as compared to air. Similar reductions are observed for other geometries and stress ranges. However, this difference is not substantial when compared to the large intrinsic variation (aleatory uncertainty) in the fatigue life.

Similar simulations with different stress ranges are performed and the fatigue life is recorded for each simulation. This allows to determine an approximation of the S–N curve. Figs. 19 and 20 compare these predicted S–N curves with the fatigue test data of Moss [9,45] on rebars in air and embedded in concrete, respectively. The data of Moss are used because they provide the largest comparative databases of fatigue test data in air and in concrete. Moss tested five different types of rebar at $R = 0.2$, of which series A and D are considered here because these are the series that contain ribs and in addition, data in both air and concrete are available for these series. Series A and D are specimen of a cold worked material and a hot rolled material, respectively. Both materials have a reported characteristic (5% fraction) yield stress of 460 N/mm^2. The corresponding expectation of the tensile strength is $f_u = 550$ N/mm^2. The mean value and standard deviation of the concrete cube strength at 28 days were 58 MPa and 4 MPa, respectively, for which a Young's modulus of $E = 3 \times 10^4$ N/mm^2. is a reasonable assumption, [46]. Material and geometric properties and test conditions as applied in the tests are also applied in the simulations. Photos of the specimen reveal a rib orientation of approximately $\theta = 45°$. Rib dimensions are not provided, so a reasonable estimate of $r/h = 0.5$ is applied in the simulations. Cold formed and hot rolled rebars may contain different residual stresses due to the shaping process. Residual stresses are not considered in the simulations.

The figures demonstrate a good agreement between the average fatigue lives of the tests and the prediction. The prediction with $D = 24$ mm is in between most failed tests data on with $D = 32$ and 40 mm bars on the one side, and $D = 16$ mm bars on the other side. The trend of the prediction, with an oblique shape instead of the often considered straight S–N curve on log–log scale, also corresponds well with the test data. The average slope parameters of the predicted S–N curves in the range 150 N/mm^2 $\leq \Delta\sigma \leq$ 350 N/mm^2 are $k_1 = -6.0$ and -5.7 for air and CMI, respectively, where k_1 is defined as:

$$k_1 = \frac{\log_{10} \Delta\sigma_1 - \log_{10} \Delta\sigma_2}{\log_{10} N_1 - \log_{10} N_2} \tag{7}$$

and subscripts 1 and 2 indicate the bounds of the previously mentioned range of $\Delta\sigma$ and the corresponding number of cycles to failure. The CMI prediction gives a slightly lower fatigue resistance as compared to the prediction in air, whereas the opposite is the case for the average test data. Considering the individual test series, it appears that the average fatigue resistance is larger in concrete than in air for Series A$\varnothing = 16$ mm, slightly larger in concrete than in air for Series A$\varnothing = 40$ mm, and almost equal for Series

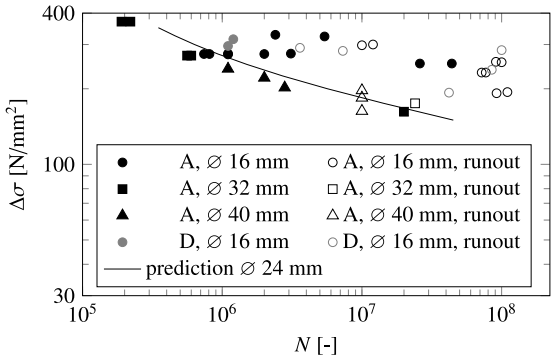

Fig. 20. Fatigue test data [9] and model prediction for rebars in concrete with $R = 0.2$.

Table 1
Fatigue life for the given geometry relative to the base geometry ($r/h = 0.5$, $\theta = 45°$) and, between brackets, relative to same geometry in air.

Case	$r/h = 0.5$ $\theta = 45°$	$r/h = 0.5$ $\theta = 60°$	$r/h = 0.5$ $\theta = 90°$	$r/h = 0.1$ $\theta = 45°$	$r/h = 0.8$ $\theta = 45°$
Air	1.	0.83	1.26	0.73	0.61
CMI	0.82 (0.82)	0.61 (0.73)	1.02 (0.81)	0.75 (1.03)	0.58 (0.95)

A∅ = 32 mm and D∅ = 16 mm. The fatigue resistance differs between Series A∅ = 16 mm and D∅ = 16 mm in air, whereas such a difference seems absent in concrete. Given that Moss' report with data in concrete was issued two years after that in air, it is possible that the rebars tested in concrete origin from other batches than those tested in air, and may have contained differences in geometry (e.g. rib radius), surface quality, and actual tensile strength. This may also have contributed to the differences tested in concrete and in air. The difference in fatigue resistance between series is larger than the difference between air and concrete embedment of a single series. In addition, the small number of tests per series in combination with the large scatter per series complicates making any conclusion on the effect of concrete embedment based on the tests.

Table 1 provides the fatigue lives predicted with the model for various geometries, as a ratio to the fatigue life of a base geometry, the latter being the geometry considered in Figs. 19 and 20, or as a ratio to the fatigue life of the same geometry in air. The average ratio between the life in concrete and the life in air is 0.87. Adopting the average slope parameter of the S–N curve of $k_1 = -5.7$, the life ratio of 0.87 is equivalent to a fatigue resistance ratio in terms of stress range of 0.98. Hence, the model predicts an insignificant difference of 2% between the fatigue resistance of rebars embedded in concrete and in air. Following Table 1, the predicted fatigue life is more sensitive to the relative rib radius than to the concrete embedment. Note that to date, standards do not prescribe any tolerance for the rib radius.

5. Discussion

Rebars are applied with lightly corroded surface both in fatigue tests and in real structures. It is well known that the fatigue resistance of unprotected steel depends on the temperature and corrosive conditions, such as humidity. These environmental conditions may influence the rebar fatigue performance in real structures with long exposure times, especially for non-embedded bars. However, the tests described in this manuscript are carried out under laboratory conditions at relatively short duration and rebars are environmentally protected by concrete in real structures. To prevent heating of the rebars due to work done during cycling, [47], this article only considered tests carried out at test frequencies of 3 Hz or less.

The predicted fatigue life is based on models containing simplifications and approximations, such as the treatment of concrete as a homogeneous material. The influence of the concrete strength has not been considered in detail. Microcracking of concrete, variation in concrete Young's modulus and fatigue of concrete depends on the concrete strength and this may in turn affect the rebar stress. Using the cohesive surface with uniform stiffness, the effects of microcracking are smeared. Concrete microcracking is particularly expected at the first ribs adjacent to the concrete tensile crack. Highest stress concentrations are then observed at the adjacent ribs. The predicted lives should therefore be treated as approximation and not as absolute values. Nonetheless, both test data and prediction model provide a small influence, if any, of the embedment in concrete on the fatigue resistance of rebars. The influence of these aspects on the fatigue strength of the rebar remains limited as long as the force is partially transferred through the ribs, Fig. 17. In the extreme case of concrete around the rebar being fully damaged, the rebar is loaded as in air, resulting into the small difference in fatigue resistance as described before.

The model allows to evaluate most of the reasons given in the past about the differences between air and embedment in concrete, refer to Section 1.

Explanation (i) for a potentially better performance in concrete due to the probability being small that the crack in concrete coincides with the weakest point in the rebar, is not likely given that the peak stress is observed at the root of the first or second

rib, with a very small difference between these two. Even the peak stress at the root of the third rib away from the concrete crack appears only marginally lower as compared to the highest peak stress. This implies that six rib roots around each concrete crack are almost equally stressed in the model containing twelve ribs in between the concrete crack. A model with a shorter distance between cracks also demonstrated that roughly 50% of the ribs are equally stressed. Given the fact that weak links are present everywhere along the surface, the probability is substantial that one of these rib roots is similar to – or even equal to – the absolute weakest link in the rebar. It is also demonstrated that the level of peak stress at the rib root is insensitive to the location of the concrete crack at or between ribs, Section 3.2. Moss [45] reported that the location of steel cracks coincides with that of concrete cracks. Question is, which of the two causes the other? Local tension stresses develop in concrete at the location of a steel crack, causing the concrete to crack at that same location.

Explanation (ii), suggesting that the steel strain reduces with increasing bond stiffness, is confirmed with the model, Fig. 16a. However, for modern rebars that contain ribs, the effect of mechanical interlock of concrete between the ribs appears important. Separating the influences of mechanical interlock and bond stiffness shows that the actual bond stiffness is not very large and, at the location of the peak stress, i.e. at the rib root, the predicted strain is not lower in concrete as compared to air. On the contrary, the model suggests that the SCF can slightly increase due to the action of concrete pressing against the ribs. Note that the cohesive strength deteriorates in fatigue and this further reduces the probability of the mentioned mechanism.

Explanation (iii) stating that concrete cracks do not fully close because of the presence of small grains in between the concrete crack faces is not studied here. It is a reasonable explanation. The second aspect of this explanation that a little slip of the rebar occurs, causing a permanent pre-compression in the steel rebar, seems less realistic for modern rebars with ribs due to the much more important influence of mechanical interlock than that of the relatively low cohesive stiffness.

The effect of a stress gradient over the height of the rebar – explanation (iv) for a better and (i) for a worse performance in concrete – is not studied here. From a mechanics point of view, the contribution is expected to be small, because of the small expected stress gradient in the rebar with the beam loaded in bending for realistic beam and rebar dimensions. A test in [48] on a bend concrete beam indicates that the crack initiates at the side of the rebar, not at the most highly stressed fibre. Westerberg's [13] explanation (ii) that a concrete crack causes local curvature in the rebar is for the same reason expected to be of minor influence.

Explanation (iii), suggesting a larger stress peak when embedded in concrete due to concrete pressing against the ribs, is confirmed with the model. This is further substantiated by two additional models, one in air and one in CMI, in which the rib flank angle α is modified from 45° to 60°. The SCF increased with 5% in air and 14% in CMI due to this modification. The modification applied in air causes a higher SCF because of the more severe rib influence whereas in concrete, it is not only the rib influence but also mechanical interlock that contributes to a higher SCF. The effect is a slightly lower predicted fatigue resistance in CMI as compared to air.

All in all, some aspects remain that may explain a slightly worse or a better rebar fatigue performance in concrete and the combined aspects may or may not compensate each-others influence. This may explain small differences observed between test series. It should also be noted that the low number of test data available per series may cause the estimate of the mean resistance to deviate from the actual value.

A potential explanation that is not provided in literature but may contribute to a better performance in concrete, is that the tensile strength of concrete is ignored when calculating the stress in the rebar. This is an obvious approximation when evaluating the ultimate resistance of the concrete beam, but in fatigue the maximum stress is lower and the concrete tensile strength may provide a contribution near the beam's neutral axis. Assuming a cyclic tensile strength of concrete of 3.8 N/mm^2 for the beam geometry and material properties of Moss' tests [9], a simple calculation based on beam theory gives a 3% lower stress in the rebar as compared to a calculation where the tensile strength is ignored. Concrete strain softening, not considered in this calculation, may further lower the rebar stress. Another potential source of influence is the interaction between the rebars in one beam. This study, as well as the studies referred to in here, considers fatigue of one rebar in a concrete beam. A system containing more rebars may perform better as compared to that of a single rebar, as tensile forces may be distributed to other rebars if one of these fails through fatigue. On the other hand, the weakest link principle may imply that the average life of a single rebar is longer as compared to the first failing rebar in an equally stressed group of rebars.

Finally, the fatigue performance of welded rebars embedded in concrete has not been studied here, [49].

6. Conclusion

The stress concentration factor (SCF) and stress intensity factor (SIF) of reinforcing rebars containing ribs in air and embedded in concrete, is studied using the finite element method. The values are applied in a prediction model to evaluate the fatigue life. A good agreement is observed between the prediction and fatigue tests carried out by others. The model is then used to evaluate the explanations given in the past about potential differences in fatigue lives of rebars when tested in air as compared to embedded in concrete. The study provides the following conclusions:

- The highest SCF is observed at the rib root, both in air and in concrete. In concrete, the SCF at the roots of the first, second and third rib away from a concrete crack are approximately equal. The locations of concrete cracks have an insignificant influence on the SCF.
- Mechanical interlock or pressure of concrete against the ribs contributes substantially to the force transfer and to the SCF at the rib root. It causes the SCF to be slightly higher in concrete as compared to air. Compared to mechanical interlock, the cohesive stiffness between concrete and steel influences the SCF only marginally for realistic cohesive stiffness values.

- Similar as for the SCF, the SIF of shallow cracks is slightly higher in concrete as compared to in air. For deep cracks the SIF in concrete is lower as compared to air because concrete restrains the lateral deformation of the rebar. However, the SIF is then already so high that this has a marginal effect on the total number of cycles.
- No large difference in fatigue resistance is predicted for rebars in air and rebars in concrete. Fatigue test generally confirm this; there seem to be about as many test campaigns showing a positive influence of concrete embedment as there are showing a negative influence. Aspects such as the material type (cold formed or hot rolled), the surface roughness, and especially the rib root radius relative to the rib height, provide a more substantial influence on the fatigue resistance as compared to concrete embedment.

Declaration of competing interest

The authors declare that they have no known competing financial interests or personal relationships that could have appeared to influence the work reported in this paper.

Acknowledgements

Elske van Heuveln is acknowledged for carrying out the pull-out test described in Section 3.1. Sjoerd Hengeveld is acknowledged for running a part of the finite element simulations. This research is not funded by 3rd parties.

Appendix. Fatigue life prediction model

The prediction model presented herein comprises a model for crack initiation and one for crack propagation. The crack initiation model depends on the tensile strength (and other variables). The tensile strength, f_u, is not mentioned for rebars used by Moss [9,45], but the nominal yield stress is reported as 460 N/mm^2 for both hot-rolled and cold formed steels. The mean yield stress is 1.077 times the nominal value (background information of EN 1992-1-1) and the mean tensile strength is approximately 10% higher than the mean yield stress. Simulations are therefore performed with f_u = 550 N/mm^2.

It is demonstrated by many that the fatigue initiation life is not only depending on the maximum stress in a notch, but also on the stress field surrounding a notch. One of the main reason is the supporting effect of the material surrounding the hot spot. This effect can be taken into account by the stress gradient method introduced by Siebel and Stieger, [50] with some modifications applied by others, e.g. [51–53], to better match the results of fatigue tests or to provide a theoretical basis for the empirical relationship between stress gradient and fatigue resistance. Because of its wide application and generally good agreement with test data, the empirical relationship in [28] is used in the initiation model applied here to compute the fatigue notch factor, K_f, from the SCF, K_t, the stress gradient, G, the type of material, and its tensile strength:

$$K_f = \frac{K_t}{1 + G^{k_1} 10^{-\left(a_G + k_2 + \frac{f_u}{b_G[MPa]}\right)}} \tag{A.1}$$

where variables a_G and b_G are given in Table A.2, constants $k_1 = 1$, 0.25 or 0.5 for $G \leq 0.1$, $0.1 < G \leq 1$ or $1 < G \leq 100$, respectively, and $k_2 = -0.5$ or 0 for $G \leq 0.1$ or $G > 0.1$, respectively.

The analyses applied in this study are obtained from linear elastic material properties. Different methods are available to estimate the cyclic stress, s, and cyclic strain, e, from the elastic notch stress, $K_f\sigma$. Neuber's method [54] is probably the most well-known, but it overestimates the cyclic stress and strain, [41]. The equivalent strain energy density method [41,55] is therefore applied. It is based on the assumption that the cyclic strain energy density at the notch is the same as determined in a linear elastic analysis:

$$\frac{\left(K_f\sigma\right)^2}{2E} = \int_0^e s\,de \tag{A.2}$$

This equation can be solved using the cyclic stress–strain curve, for which the Ramberg–Osgood relationship [56] is adopted:

$$e = \frac{s}{E} + \left(\frac{s}{K'}\right)^{1/n'} \tag{A.3}$$

Combining and integrating Eqs. (A.2) and (A.3) provides the following relationships for the maximum cyclic stress and the cyclic stress range:

$$\frac{\left(K_f\sigma_{max}\right)^2}{2E} = \frac{s_{max}^2}{2E} + \frac{s_{max}}{n'+1}\left(\frac{s_{max}}{K'}\right)^{1/n'} \tag{A.4}$$

$$\frac{\left(K_f\Delta\sigma\right)^2}{2E} = \frac{(\Delta s)^2}{2E} + 2\frac{\Delta s}{n'+1}\left(\frac{\Delta s}{2K'}\right)^{1/n'} \tag{A.5}$$

Parameters n' and K' are estimated from the strain-life relationship for crack initiation. The adopted strain-life relationship is a well-known relationship by Coffin–Manson [43] for relatively high strain amplitude and short endurance, combined with Basquin's log–log relationship [42] for relatively low strain amplitude and long endurance. The relation is valid for fully reversed cycles and must be modified to account for the effect of mean stress. Amongst widely applied mean stress modifications such as those of

Table A.2
Material related variables in the fatigue life prediction model (units N, mm).

Symbol	Description	Value	Source
a_G	Stress gradient constant	0.5	[28]
b_G	Stress gradient constant	2700.	[28]
s'_f	High cycle regime constant	$(4.25H_b + 225)$	[57]
b	High cycle regime exponent	−0.09	[58]
e'_f	Low cycle regime constant	$(0.32H_b^2 - 487H_b + 191000)/E$	[57]
c	Low cycle regime exponent	−0.56	[58]
N_0	Fatigue limit (plain mat.)	10^6	[59]
k_a	Surface roughness factor	$69f_u^{-0.743}$[a]	[59]
C_1	Crack growth constant	1.2×10^{-26}	[37]
m_1	Crack growth exponent	8.16	[37]
C_2	Crack growth constant	3.9×10^{-13}	[37]
m_2	Crack growth exponent	2.88	[37]

[a]Valid for material with mill scale.

Soderberg, Goodman, Gerber and Dietman (e.g. [60]) and Smith et al. [61], this work adopts the modified Morrow mean stress equation [44] because of its good performance for high strength metals, relevant for the materials constituting modern rebars. The combined Coffin–Manson, Basquin and Morrow fatigue life initiation equation is:

$$e_a = \frac{s'_f - s_m}{E}\left(2N_i\right)^{b'} + e'_f\left(2N_i\right)^{c} \tag{A.6}$$

$$n' = b/c \tag{A.7}$$

$$K' = \frac{s'_f}{\left(e'_f\right)^{n'}} \tag{A.8}$$

where:

e_a = cyclic strain amplitude caused by the load cycle, Eq. (A.9)
s_m = average cyclic stress caused by the load cycle ($s_m = s_{max} - 0.5\Delta s$)
N_i = number of cycles to crack initiation
s'_f = constant in the high cycle regime, Table A.2
b = exponent in the high cycle regime, Table A.2
b' = exponent in the high cycle regime, corrected for surface roughness
e'_f = constant in the low cycle regime, Table A.2
c' = exponent in the low cycle regime, Table A.2.

Most sources correlate variables s'_f and e'_f to Brinell hardness, H_b. The hardness is estimated from the tensile strength: $H_b = f_u/(345\ \text{MPa})$.

$$e_a = \frac{\Delta s}{2E} + \left(\frac{\Delta s}{2K'}\right)^{1/n'} \tag{A.9}$$

The difference between parameter b in Eq. (A.7) and b' in Eq. (A.6) is that the latter accounts for the effect of the surface roughness. It is assumed here that the surface condition only affects the high cycle fatigue regime. Parameter b' can be estimated from b:

$$b' = b + \frac{\log_{10}\left(k_a\right)}{\log_{10}\left(2N_0\right)} \tag{A.10}$$

where N_0 is the endurance limit for plain material and k_a is a correlation factor for surface roughness and tensile strength, Different empirical relationships are proposed in literature to account for k_a, i.e. the surface roughness, such as [28,62–64]. Most of them require an actual measured quantity for the surface roughness, but such measurements are not available for the experimental data of Moss [9,45] and many others. Mischke formulates his surface roughness dependency of the fatigue limit more generically on the type of processing, such as grinding, hot-rolling, or as-forged. His relationship is therefore adopted in k_a for the as-received surface condition for rolling.

Eq. (A.6) is used to estimate N_i. The material dependent parameters in Table A.2 are typically calibrated from tests on plain material with a first visual crack and the corresponding crack size may vary. Based on our experience, it is assumed here that the visually detectable crack size is on average 0.5 mm. Linear elastic fracture mechanics is used to estimate the crack propagation life

from that crack size onwards. The two-stage relation from BS 7910:2019 [37] is used to evaluate the crack extension per cycle, da/dN, as a function of the SIF range, ΔK:

$$da/dN = \min\left(C_1 \Delta K^{m_1}, C_2 \Delta K^{m_2}\right) \tag{A.11}$$

where C_1, m_1 and C_2, m_2 are the crack growth constants and exponents for small and large SIF ranges, respectively, with values according to Table A.2. Propagation is simulated up to a relative crack size of $a/D = 0.5$, after which a large growth rate or fracture is assumed.

Section 4 compares the results of the prediction model to test data on reinforcement bars. As a further verification of the model, test data in [48] on rebars and machined specimens taken from those rebars are compared to the prediction. The measured tensile strength f_u of the specimens was 750 MPa. The model is modified for machined specimen by taking $K_f = 1$, Y according to [29], and $k_a = 4.51 f_u^{-0.265}$ according to [59]. The predicted difference in fatigue resistance between the rebar and the machined specimen at $N = 10^6$ is 255 MPa. This is close to the difference reported for the tests, which is 241 MPa (35 ksi) at the same number of cycles.

References

[1] Helagson T, Hanson JM. Investigation of design factors affecting fatigue strength of reinforcing bars-statistical analysis. Special Publ 1974;41:107–38.
[2] MacGregor JG, Jhamb IC, Nuttall N. Fatigue strength of hot rolled deformed reinforcing bars. J Proc 1971;68:169–79.
[3] Thorsteinn H, Hanson JM, Somes NF, Corley WG, Hognestad E. Fatigue strength of high-yield reinforcing bars. National cooperative highway research program; 1976.
[4] Soltani A, Harries KA, Shahrooz BM, Russell HG, Miller RA. Fatigue performance of high-strength reinforcing steel. J Bridge Eng 2012;17:454–61.
[5] Hanson JM, Ballinger CA. Considerations for design of concrete structures subjected to fatigue loading, ACI 215R-74. ACI; 1997.
[6] Rocha Pinto Portela Nunes M. Fatigue behaviour of steel reinforcement bars at very high number of cycles (EPFL thesis no. 6382(2014)), EPFL; 2014.
[7] Corley W, Helgason T, Hanson JM. Design of reinforced concrete for fatigue. J Struct Div 1978;104:921–32.
[8] Daoud OEK, Lovegrove JM. The effect of concrete bond on the stress intensity factors for an edge crack in a reinforcing bar. Fatigue Eng Mater Struct 1983;6:257–69.
[9] Moss DS. Bending fatigue of high-yield reinforcing bars in concrete. Transport and Road Research Laboratory,Crowthorne; 1982.
[10] Jhamb I, McGregor J. Effect of surface characteristics on fatigue strength of reinforcing steel. ACI Special Publ 1974;41:139–68.
[11] Soretz S. Fatigue behavior of high yield steel reinforcement. Concrete Constr Eng 1965;60:272–80.
[12] Rehm G. Contributions to the problem of the fatigue strength of steel bars for concrete reinforcement. In: International Association for Bridge and Structural Engineering (IABSE), Vol. 6. 1960, p. 35–46.
[13] Westerberg B, Jacobson A. Fatigue properties of reinforced concrete structures, In: Proc. 1st Int. Conf. Behavior of Off-Shore Structures, 1976: p. 140–174.
[14] Tilly G. Fatigue of steel reinforcement bars in concrete: a review. Fatigue Eng Mater Struct 1979;2:251–68.
[15] Bannister JL. Fatigue resistance of reinforcement for concrete. In: Proc. Underwater Construction Technology. University College, Cardiff; 1975, p. 1.
[16] Walker EF, Austen IM, Harrison TC, Morley J. Fatigue and corrosion fatigue of reinforcement bars. In: Proceedings Underwater Construction Technology. University College, Cardiff; 1975, p. 1.
[17] Remitz J, Empelmann M. Cyclic tensile tests on prestressing strands embedded in concrete. Mater Struct 2020;53:1–15.
[18] Bosse H. Schäden an Fundamenten von Windenergieanlagen treten vermerht auf. Wind Wissens Tech Erneu Energien 2009;February:24–30.
[19] Chen J, Xu Y, Li J. Numerical investigation of the strengthening method by circumferential prestressing to improve the fatigue life of embedded-ring concrete foundation for onshore wind turbine tower. Energies 2020;13:1–17.
[20] Suthiwarapirak P, Matsumot T. Fatigue analysis of RC slabs and repaired RC slabs based on crack bridging degradation concept. J Struct Eng 2006;132:939–48.
[21] Zheng H, Abel A. Stress concentration and fatigue of profiled reinforcing steels. Int J Fatigue 1997;20:767–73.
[22] Lovegrove JM, Salah El Din AS, Daoud OEK. Fatigue crack growth in the tension steel of reinforced concrete. Fatigue Eng Mater Struct 1979;1:173–83.
[23] Barsom JM. Fatigue crack propagation in steels of various yield strength. J Eng Ind 1971;93:1190–6.
[24] Pfister J, Hognestad E. High strength bars as concrete reinforcement: fatigue tests. J PCA Res Devel Lab 1964;6:65–84.
[25] Jhamb I, McGregor J. Stress concentration caused by reinforcing bar deformations. ACI Special Publ 1974;41:169–82.
[26] CEN. EN 10080:2005 Steel for the reinforcement of concrete - Weldable reinforcing steel - General. CEN; 2005.
[27] Neuber H. Kerbspannungslehre, Theorie der Spannungskonzentration Genaue Berechnung der Festigkeit. Springer; 2001.
[28] Hänel B, Haibach E, Seeger T. Analytical strength assessment of components made of steel, cast iron and aluminium materials in mechanical engineering. Forschungskuratorium Maschinenbau – VDMA Verlag; 2012.
[29] Forman RG, Shivakumar V. Growth behavior of surface cracks in the circumferential plane of solid and hollow cylinders. In: Fracture Mechanics: Seventeenth Volume, ASTM STP 905. ASTM; 1986, p. 59–74.
[30] James LA, Mills WJ. Review and syntesis of stress intensity factor solutions applicable to cracks in bolts. Eng Fract Mech 1988;30:641–54.
[31] Raju IS, Newman JC. Stress-intensity factors for circumferential surface cracks in pipe and rods under tension and bending loads.. In: Fracture Mechanics: Seventeenth Volume, ASTM STP 905. ASTM; 1986, p. 789–805.
[32] Chu SF, Kwan AKH. A new method for pull out test of reinforcing bars in plain and fibre reinforced concrete. Eng Struct 2018;164:82–91.
[33] Ruiz WM, Winter G. Reinforced concrete beams under repeated loads. J Struct Div 1969;95:1189–211.
[34] Balázs GL. Fatigue of bond. ACI Mater J 1991;1991:620–9.
[35] Nagesh HE, Appa Rao G. Fatigue behavior of lightly reinforced concrete beams in flexure due to overload. In: Saouma V, Bolander J, Landis E, editors. 9th International Conference on Fracture Mechanics of Concrete and Concrete Structures, Vol. 9. 2016, p. 1–12.
[36] Balázs GL. Connecting reinforcement to concrete by bond. Beton Stahlbetonbau 2007;102:46–50.
[37] BSI. BS 7910:2019 Guide to methods for assessing the acceptability of flaws in metallic structures. BSI; 2019.
[38] Maljaars J, Leonetti D, Maas C. Fatigue life prediction of hot riveted double covered butt joints. Int J Fatigue 2019;124:99–112.
[39] Leonetti D, Maljaars J, Snijder H. Fatigue life prediction of hot-riveted shear connections using system reliability. Eng Struct 2019;186:471–83.
[40] De Jesus AMP, Pinto H, Fernández-Canteli A, Castilloc E, Correia JAFO. Fatigue assessment of a riveted shear splice based on a probabilistic model. Int J Fatigue 2010;32:453–62.
[41] Molski K, Glinka G. A method of elastic-plastic stress and strain calculation at a notch root. Mater Sci Eng 1981;50:93–100.
[42] Basquin OH. The exponential law of endurance test. Proc Amer Soc Test Mater 1910;10:625–30.
[43] Manson SS. Fatigue: a complex subject – some simple approximations. Exp Mech 1965;5:193–226.
[44] Morrow J. Fatigue properties of metals. In: Fatigue Design Handbook. SAE; 1968, p. 21–9.
[45] Moss DS. Axial fatigue of high-yield reinforcing bars in air. Transport and Road Research Laboratory,Crowthorne; 1980.

[46] Noguchi T, Tomosawa F. Relationship between compressive strength and modulus of elasticity of high-strength concrete. J Struct Constr Eng (Trans AIJ) 1995;60:1–10.
[47] Mallet GP. Fatigue of reinforced concrete. HMSO Publications Centre, London; 1991.
[48] Helgason T, Hanson JM, Somes NF, Corley WG, Hognestad E. Fatigue Strength of High Yield Reinforcing Bars, NCHRP Bulletin 164. Transportation Research Board; 1976.
[49] Sanders WW, Hoadley PG, Munse WH. Fatigue behavior of welded joints in reinforcing bars for concrete. Welding J Res Suppl 1961;40:529s–35s.
[50] Siebel E, Stieler M. Ungleichförmige Spannungsverteilung bei schwingender Beanspruchung. Z Ver Deutsch Ing 1955;97:121–31.
[51] Eichlseder W. Fatigue analysis by local stress concept based on finite element results. Comput Struct 2002;80:2109–13.
[52] Zhang G. Method of effective stress for fatigue: part I—a general theory. Int J Fatigue 2012;37:17–23.
[53] Mei J, Xing S, Vasu A, Chung J, Desai R, Dong P. The fatigue limit prediction of notched components—a critical review and modified stress gradient based approach. Int J Fatigue 2020;135:1–15.
[54] Neuber H. Kerbspannungslehre Grundlagen für genaue Festigkeitsberechnung mit Berücksichtigung von Konstruktionsform und Werkstoff. second ed.. Springer Berlin Heidelberg; 1958.
[55] Glinka G. Calculation of inelastic notch-tip strain-stress histories under cyclic loading. Eng Fract Mech 1985;22:839–54.
[56] Ramberg W, Osgood WR. Description of stress-strain curves by three parameters. Technical note 902, NASA; 1943.
[57] Roessle ML, Fatemi A. Strain-controlled fatigue properties of steels and some simple approximations. Int J Fatigue 2000;22:495–511.
[58] Meggiolaro MAA, Castro JTP. Statistical evaluation of strain-life fatigue crack initiation predictions. Int J Fatigue 2004;26:463–76.
[59] Mischke CR. Prediction of stochastic endurance strength. J Vib Acoust Stress Reliab 1987;109:113–22.
[60] Susmel L, Tovo R, Lazzarin P. The mean stress effect on the high-cycle fatigue strengthfrom a multiaxial fatigue point of view. Int J Fatigue 2005;27:928–43.
[61] Smith KN, Watson P, Topper TH. A stress-strain function for the fatigue of metals. J Mater 1970;5:767–78.
[62] Alang NA, Razak NA, Miskam AK. Effect of surface roughness on fatigue life of notched carbon steel. Int J Eng Technol 2011;11:160–3.
[63] Itoga H, Tokaji K, Nakajima M, Ko HN. Effect of surface roughness on step-wise S–N characteristics in high strength steel. Int J Fatigue 2003;25:379–85.
[64] Novovic D, Dewes RC, Aspinwall D, Voice W, Bowen P. The effect of machined topography and integrity on fatigue life. Int J Mach Tools Manuf 2004;44:125–34.